arXiv:1403.4935v1 [astro-ph.GA] 19 Mar 2014

Accepted to the ApJ

Spectral Energy Distribution Fitting of HETDEX Pilot Survey Lyα Emitters in COSMOS and GOODS-N

Alex Hagen[1,2], Robin Ciardullo[1,2], Caryl Gronwall[1,2], Viviana Acquaviva[3], Joanna Bridge[1,2], Gregory R. Zeimann[1,2], Guillermo A. Blanc[4], Nicholas A. Bond[5], Steven L. Finkelstein[6], Mimi Song[6], Eric Gawiser[7], Derek B. Fox[1,2], Henry Gebhardt[1,2], A.I. Malz[1,2], Donald P. Schneider[1,2],

hagen@psu.edu

ABSTRACT

We use broadband photometry extending from the rest-frame UV to the near-IR to fit the *individual* spectral energy distributions (SEDs) of 63 bright ($L(\mathrm{Ly}\alpha) > 10^{43}$ ergs s^{-1}) Lyα emitting galaxies (LAEs) in the redshift range $1.9 < z < 3.6$. We find that these LAEs are quite heterogeneous, with stellar masses that span over three orders of magnitude, from $7.5 < \log M/M_\odot < 10.5$. Moreover, although most LAEs have small amounts of extinction, some high-mass objects have stellar reddenings as large as $E(B-V) \sim 0.4$. Interestingly, in dusty objects the optical depths for Lyα and the UV continuum are always similar, indicating that Lyα photons are not undergoing many scatters before escaping their galaxy. In contrast, the ratio of optical depths in low-reddening systems can vary widely, illustrating the diverse nature of the systems. Finally, we show that in the star formation rate (SFR)-log mass diagram, our LAEs fall above the "main-sequence" defined by $z \sim 3$ continuum selected star-forming galaxies. In this respect, they are similar to sub-mm-selected galaxies, although most LAEs have much lower mass.

Subject headings: galaxies: evolution – galaxies: high-redshift – galaxies: masses – cosmology: observations

[1]Department of Astronomy & Astrophysics, The Pennsylvania State University, 525 Davey Lab, University Park, PA 16802

[2]Institute for Gravitation and the Cosmos, The Pennsylvania State University, University Park, PA 16802

[3]Department of Physics, New York City College of Technology, City University of New York, 300 Jay Street, Brooklyn, NY 11201

[4]Observatories of the Carnegie Institution for Science, Pasadena, CA 91101

[5]Cosmology Laboratory, NASA Goddard Space Flight Center, Greenbelt, MD 20771

[6]Department of Astronomy, The University of Texas at Austin, Austin, TX, 78712

[7]Department of Physics and Astronomy, Rutgers, The State University of New Jersey, Piscataway, NJ 08854

[8]Department of Astronomy, The University of Texas at Austin, Austin, TX, 78712

1. Introduction

Patridge & Peebles (1967) originally predicted that the Lyα emission line could be a very useful probe of the high-redshift universe, and, while it took many years to detect this feature (Cowie & Hu 1998; Hu et al. 1998), Lyα emitting galaxies (LAEs) are now routinely observable from $z \sim 0.2$ (Deharveng et al. 2008; Cowie et al. 2010) to $z > 7$ (Hu et al. 2010; Ouchi et al. 2010; Lidman et al. 2012; Ono et al. 2012). However, while the detection of Lyα in the high-redshift universe is relatively common, the physics of this emission is still not well understood. Since Lyα is a resonance transition, it is likely that each photon scatters many times off intervening neutral material before escaping into intergalactic space. As a result, even a small amount of dust should extinguish the line, and indeed, only $\sim 25\%$ of Lyman-break galaxies (LBGs) at $z \sim 2-3$ have enough Lyα in emission to be classified as an LAE (Shapley et al. 2003). While it is possible for dusty galaxies to create an escape path for Lyα via supernova-blown bubbles and/or exotic geometry (e.g., Verhamme et al. 2012) most analyses suggest that the LAE population as a whole is made up of young, low-mass, low-metallicity systems, possessing relatively little interstellar dust (e.g., Gawiser et al. 2007; Guaita et al. 2011).

To date, most Lyα emitters have been detected via deep narrow-band imaging with 4-m and 8-m class telescopes (e.g., Gronwall et al. 2007; Ouchi et al. 2008) . These surveys generally extend to low Lyα luminosities and sample a wide range of the high-redshift galaxy luminosity function. Unfortunately, in the continuum, LAEs are usually quite faint, which makes studying their spectral energy distributions (SEDs) difficult. As a result, most of our knowledge about those physical properties which are encoded in the objects' SEDs – information such as stellar mass, extinction, and population age – has come from stacking techniques (e.g., Gawiser et al. 2007; Guaita et al. 2011). These analyses only yield estimates for a "typical" LAE and may be subject to serious systematic biases associated with the stacking techniques (Vargas et al. 2014). Moreover, those few programs that have sought to measure the SEDs of individual LAEs (e.g., Finkelstein et al. 2009; Nilsson et al. 2011; Yuma et al. 2010; Nakajima et al. 2012; McLinden et al. 2014) have generally been restricted to very small numbers of objects. These efforts have been able to provide hints as to the range of properties exhibited by the population, but have been unable to probe the statistics of the entire LAE population. Thus, while we have some idea about the mass and dust content of "representative" LAEs, the distribution of physical parameters for the entire population remains poorly constrained.

Here, we investigate the stellar populations of luminous Lyα emitters by analyzing the individual spectral energy distributions of 63 $1.9 < z < 3.6$ LAEs detected by the McDonald 2.7-m telescope's Hobby-Eberly Telescope Dark Energy Experiment (HETDEX) Pilot Survey. In Section 2, we summarize the HETDEX Pilot Survey and describe the ancillary groundbased, *HST*, and *Spitzer* photometry which is available for analysis. In Section 3, we briefly describe the SED-fitting code `GalMC` (Acquaviva et al. 2011) and the underlying assumptions used to derive stellar mass, extinction, and age from a set of broadband photometry which extends from the rest-frame UV through to the near-IR. We also outline the procedures used to measure the physical sizes of

the LAEs in a manner that is insensitive to the effects of cosmological surface brightness dimming. In Section 4, we present our results and show that the population of luminous $z \sim 3$ LAEs is quite heterogeneous, with sizes extending from 0.5 kpc $\lesssim r \lesssim$ 4 kpc, stellar masses ranging from $7.5 < \log M/M_{\odot} < 10.5$, and differential extinctions varying between $0.0 < E(B-V) < 0.4$. We illustrate several trends involving LAE physical parameters, including a positive correlation between reddening and stellar mass, a positive correlation between stellar mass and galactic age, and a positive correlation between galaxy size and Lyα luminosity. We also examine the possible evolution of physical properties with redshift and compare our LAEs to other $z \sim 3$ objects on the star-forming galaxy main sequence. We conclude by discussing the implications of our results for the underlying physical mechanisms of Lyα escape in high redshift galaxies.

For this paper we adopt a cosmology with $H_0 = 70$ km s^{-1} Mpc^{-1}, $\Omega_{\rm M} = 0.3$, and $\Omega_{\Lambda} = 0.7$ (Planck Collaboration 2013; Hinshaw et al. 2013).

2. Our Sample

The LAEs chosen for study were discovered with the George & Cynthia Mitchell Spectrograph (previously known as VIRUS-P; Hill et al. 2008) on the 2.7-m Harlan J. Smith Telescope during the HETDEX Pilot Survey (HPS; Adams et al. 2011). This integral-field instrument, which employs an array of 246 4.″2 diameter fibers, covers ~ 3 arcmin^2 of sky at a time, and delivers 5 Å resolution spectra between the wavelengths 3500 Å and 5800 Å. The HPS itself surveyed a total of 169 arcmin^2 in the COSMOS (Scoville et al. 2007a), GOODS-N (Giavalisco et al. 2004), MUNICS-S2 (Drory et al. 2001), and XMM-LSS (Pierre et al. 2004) fields and reached a limiting line flux of 6.7×10^{-17} ergs cm^{-2} s^{-1} at 5000 Å (for 50% of its pointings) and 1.0×10^{-16} ergs cm^{-2} s^{-1} at 5000 Å (for 90% of the pointings). The final HPS catalog consists of coordinates, redshifts, R-band magnitudes, line fluxes, and equivalent widths for 397 emission-line selected galaxies. Ninty-nine of these sources are non X-ray emitting LAEs with $1.9 < z < 3.8$, rest-frame equivalent widths EW$_0 > 20$ Å, and Lyα luminosities between 2.6×10^{42} and 1.1×10^{44} ergs s^{-1} (Adams et al. 2011; Blanc et al. 2011). A total of 74 of these HPS LAEs lie in the GOODS-N and COSMOS fields, where deep *HST* data is available. The redshift range for this subsample is $1.9 < z < 3.6$.

The process of assigning an optical counterpart to each HPS emission-line detection was challenging. As pointed out by Adams et al. (2011), there is an order of magnitude mismatch between the spatial resolution obtained from the 4.″2 diameter fibers of VIRUS-P, and that delivered by the broadband imagers of *HST*. Thus, each assignment was done in a Bayesian manner, by calculating the likelihood of association for each object within a 10″ window of the nominal position obtained from the spectroscopy (see Section 5.3 of Adams et al. 2011). Formally, the median probability for identifying the correct optical counterpart was 64%. However, as discussed below in the final paragraph of Section 3.1, there is no statistical difference between the distribution of SED properties for a sample LAEs with high-probability and/or confirmed counterparts and that for the sample of lower-probability associations.

In total, we identified 67 HPS LAEs with optical counterparts. Four of these objects (HPS IDs 144, 145, 160, and 196) were removed from our analysis based on the work of Blanc et al. (2011), who showed that their UV slopes were more consistent with those of foreground [O II] emitters than LAEs. This culling left us with 63 objects for analysis. Since the X-ray data in GOODS-N and COSMOS is deep enough to rule out most AGN, we believe that the bulk **of** these objects are true Lyα emitting sources with $1.9 < z < 3.6$ and monochromatic Lyα luminosities between 3.4×10^{42} and 3.8×10^{43} ergs s^{-1}.

Before proceeding further, we should note that the LAEs discovered by the HPS are significantly more luminous than the Lyα emitters found by most narrow-band surveys. While the $2 < z < 3$ observations of Gronwall et al. (2007), Ouchi et al. (2008), and Guaita et al. (2010) typically reach Lyα 90% completeness levels of $L(\mathrm{Ly}\alpha) \sim 10^{42}$ ergs s^{-1}, the median HPS limit is five times brighter than this. On the other hand, since the Lyα luminosity limit of the HPS is very nearly constant across the survey's entire spectral range (see Figure 1 of Blanc et al. 2011), the data set covers an order of magnitude more co-moving volume than a typical narrow-band survey, with $V = 5.63 \times 10^5$ Mpc^3 in the COSMOS and GOODS-N regions alone. This allows us to obtain good statistics on the bright end of the LAE population, and explore evolution over ~ 1.6 Gyr of cosmic time.

The HPS fields, and in particular, the COSMOS and GOODS-N regions are rich in deep, ancillary imaging and provide up to 18 photometric data points for SED fitting. Tables 1 and 2 summarize these data. Most of the HPS/COSMOS and HPS/GOODS-N fields are part of CANDELS (Grogin et al. 2011; Koekemoer et al. 2011), and 49 out of our 63 LAEs have deep *HST* optical and near-IR photometry (Song et al. 2013; Finkelstein et al. 2013) from this program. Moreover, all of our targets have photometry from Adams et al. (2011), who used the deep ground-based images of COSMOS as their source frames (Capak et al. 2007). Note that many of the LAEs targeted in this survey are too faint in the continuum to be present in the published COSMOS and GOODS photometric catalogs; for these objects, AB magnitudes were determined by re-measuring the original images using the positions of the *HST* optical counterparts. Still, there are some non-detections. When this occurred, an upper flux limit was assigned as the $1\,\sigma$ uncertainty of the local sky value. In some cases, these limits were crucial for constraining the SED properties of our targets.

Data at longer wavelengths come from observations with the Spitzer telescope. Once again, most LAEs are far too faint to be present in the S-COSMOS and GOODS-N Spitzer catalogs, as these analyses have relatively high detection thresholds (1 μJy in IRAC channel 1). Since the rest-frame near-IR is extremely important for determining stellar mass, we performed our own aperture photometry on these frames using MOPEX[1] (Makovoz & Marleau 2005) at the known LAE positions. After experimenting with a variety of apertures, we settled on a photometric radius

[1]Information on MOPEX is available at `http://irsa.ipac.caltech.edu/data/SPITZER/docs/dataanalysistools/tools/mopex/`

of 3.″6, and then applied an aperture correction as described in the IRAC Instrument Handbook[2].

3. Data Analysis

3.1. Spectral Energy Distribution Fitting

The spectral energy distribution of a galaxy encodes a number of physical parameters, including stellar mass, age, dust content, and the current star formation rate (SFR). For example, since a galaxy's near-IR flux arises principally from the evolved stars of all stellar populations, that part of the SED traces the system's total stellar mass (Bell & de Jong 2001; Zibetti et al. 2009). In contrast, the slope of a galaxy's far UV ($\sim$ 1600 Å) continuum is fixed by the Rayleigh-Jeans tail of the blackbody emission from hot, young stars. The amplitude of the UV continuum thus yields the star formation rate and any flattening of the UV continuum's slope is most likely due to the effects of dust (Kennicutt 1998; Calzetti 2001). Estimates of population age come primarily from the regions in between, as features such as the Balmer and 4000 Å breaks are sensitive to the main sequence turnoff and the exact mix of intermediate age stars (e.g., Kauffmann et al. 2003).

To extract this information, we began with the population synthesis models of Bruzual & Charlot (2003), which were updated in 2007 (BC07) with an improved treatment of the thermal-pulsing asymptotic giant branch (TP-AGB) phase of stellar evolution. This phase of stellar evolution can be important for systems older than $\sim 10^8$ years, which is $\sim 30\%$ of our sample (see Section 4.4). We also performed fits using the older BC03 models, but due to the generally young ages of the stellar populations, these fits were statistically indistinguishable from the 2007 models. For the remainder of this paper, we will only refer to our BC07 results. For consistency with the works of Guaita et al. (2011) and Acquaviva et al. (2011), we adopted a Salpeter (1955) initial mass function (IMF) over the range $0.1 M_\odot < M < 100\,M_\odot$, a Calzetti (2001) extinction law, and a Madau (1995) model for the effects of intervening intergalactic absorption. Since stellar metal abundances are poorly constrained by broadband SED measurements, we fixed the metallicity of our models to $Z = 0.2\,Z_\odot$; this is roughly the gas-phase abundance inferred from recent near-IR spectroscopy of $z \sim 2$ LAEs (Nakajima et al. 2013; Song et al. 2013). Emission lines and nebular continuum, which can be an important contributor to the broadband SED of high-z galaxies (e.g., Atek et al. 2011; Schaerer & de Barros 2009), were modeled following the prescription of Acquaviva et al. (2011) with updated templates from Acquaviva (2012). Finally, following Guaita et al. (2011), we adopted the simple assumption that the SFRs of our LAEs have been constant with time.

In keeping with these assumptions, we did not use any of the bandpasses listed in Tables 1 and 2 that lie redward of 3.3 μm in the rest-frame. This is where the first PAH line is located, and such ISM features are not accounted for in the stellar populations models. We also did not use

[2]http://irsa.ipac.caltech.edu/data/SPITZER/docs/irac/iracinstrumenthandbook/28/

data bluewards of Lyα, as the Madau (1995) correction is statistical in nature, and large excursions from the norm could bias our reddening measurements.

Since SED fitting is a notoriously non-linear problem that may involve many local minima, highly non-Gaussian errors, and degeneracies between parameters, we chose to analyze our data using `GalMC`, a Markov-Chain Monte-Carlo (MCMC) code with a Metropolis-Hastings sampler (Acquaviva et al. 2011). This approach is much more computationally efficient than traditional grid searches, as it explores all regions of parameter space, while still spending the bulk of its time in the highest-likelihood parts of the probability distribution. The uncertainties associated with the fitted parameters are also much more realistic than those estimated using a simple χ^2 minimization, as degeneracies between the variables are bettered explored and quantified. For each SED, three free parameters, stellar mass, $E(B-V)$, and age (which, under the assumption of a constant SFR history, is equivalent to star formation rate), were fit using four chains initiated from random starting locations. Once completed, the chains were analyzed via the `CosmoMC` program `GetDist` (Lewis & Bridle 2002), and, since multiple chains were computed for each object, the Gelman & Rubin (1992) R statistic was used to test for convergence using the criterion $R-1<0.1$ (Brooks & Gelman 1998).

As discussed at length by Conroy (2013), the results of our fits should be robust within the context of our model assumptions. Of course, any change to these assumptions will result in a systematic error. For example, the use of a Chabrier (2003) or Kroupa (2001) IMF would systematically reduce our stellar mass estimates by ~ 0.3 dex, while leaving our values for extinction and age essentially unchanged (Papovich et al. 2011). Similarly, a different treatment of the TP-AGB phase may change the stellar mass estimates by up to ~ 0.3 dex (Zibetti et al. 2009), while a shift to solar metallicity will generally increase our masses by ~ 0.1 dex. A full discussion of these systematic uncertainties is given by Conroy (2013).

Figure 1 demonstrates the effectiveness of our fits by comparing the broadband photometry to the best fit SED for HPS 189. Since our data contain many bands of photometry, the SEDs of our galaxies are generally well constrained. Table 3 summarizes the SED-based properties of all 63 LAEs in our sample.

As stated in Section 2, the assignment of optical counterparts to the HPS-discovered emission lines is probabilistic in nature. To investigate this further, we constructed a "clean" sample of HPS-LAEs, using a set of 29 candidates with either spectroscopic confirmations (Finkelstein et al. 2011; Chonis et al. 2013; Song et al. 2013) or a very high (≥ 0.9) probability of association. We then used the Kolmogorov-Smirnov statistic to test whether the sample's distributions of stellar mass, age, and reddening were in any way different from those formed from the remaining 34 LAEs. Figure 2 compares the empirical cumulative distribution functions (ECDFs) of the samples for all three SED parameters. In all cases, the two distributions are statistically indistinguishable. Misidentifications are therefore not biasing the results of our SED fitting.

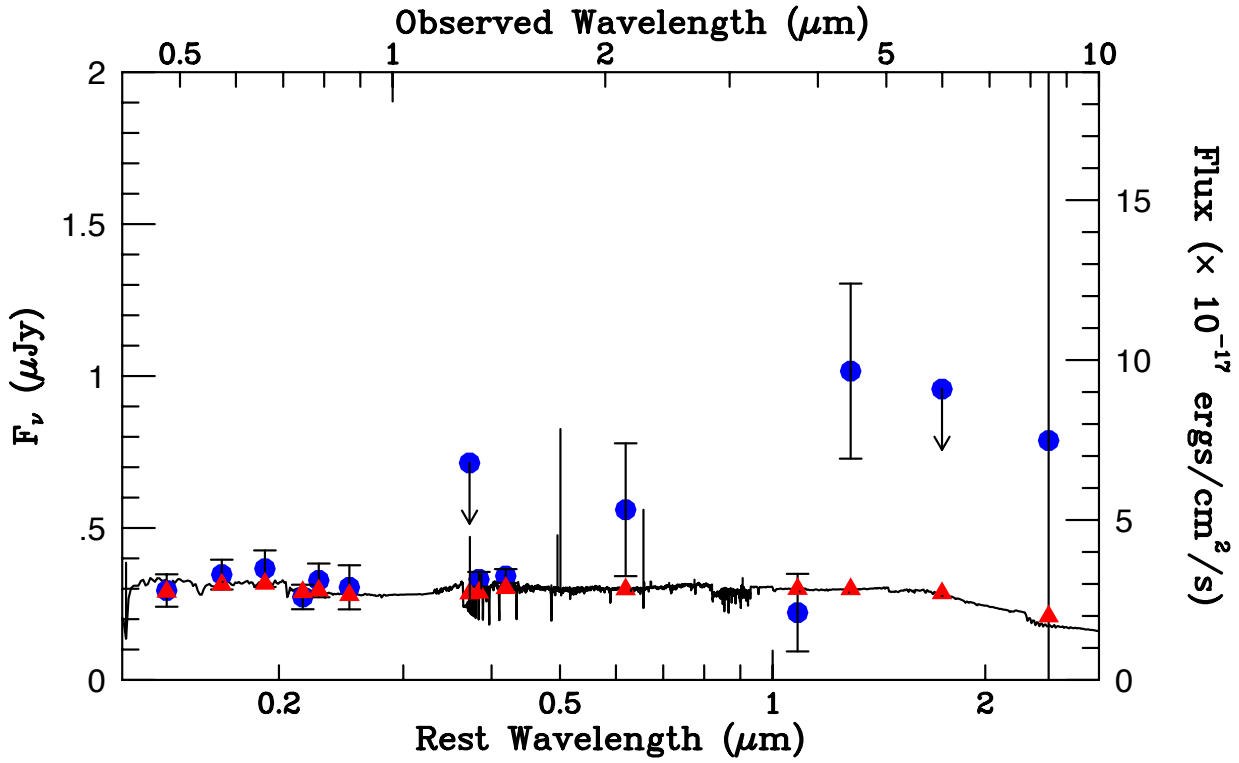

Fig. 1.— The results of our SED fit to the photometry of HPS189. The blue points are the observed flux densities, the black line is the best fit SED, and the red triangles show the predicted flux density within each band. The left axis defines the scaling for the galactic continuum; the right axis gives the monochromatic flux scale applicable to the emission lines.

3.2. Size Measurements

To complement our SED-based estimates of stellar mass, extinction, and age, we also measured the sizes of the LAEs' star-forming regions, via rest-frame UV measurements from *HST*. In the COSMOS field, deep F814W images are available, which, for the LAEs targeted in this study, sample the rest-frame wavelength region between $\sim$ 2100 Å and $\sim$ 2800 Å, depending on redshift. For GOODS-N LAEs, we have access to F606W observations, which are sensitive to rest-frame wavelengths from $\sim$ 1600 Å to $\sim$ 2100 Å. In both cases, we followed the exact same procedures described in Section 3.2 of Bond et al. (2009). After creating cutouts around each galaxy, we performed object identifications and background subtraction using the routines found in SExtractor (Bertin & Arnouts 1996). We then obtained a measure of size by using the IRAF[3] program `phot` to determine each object's flux-weight centroid and magnitude through a series of circular apertures.

[3]IRAF is distributed by the National Optical Astronomy Observatories, which are operated by the Association of Universities for Research in Astronomy, Inc., under cooperative agreement with the National Science Foundation.

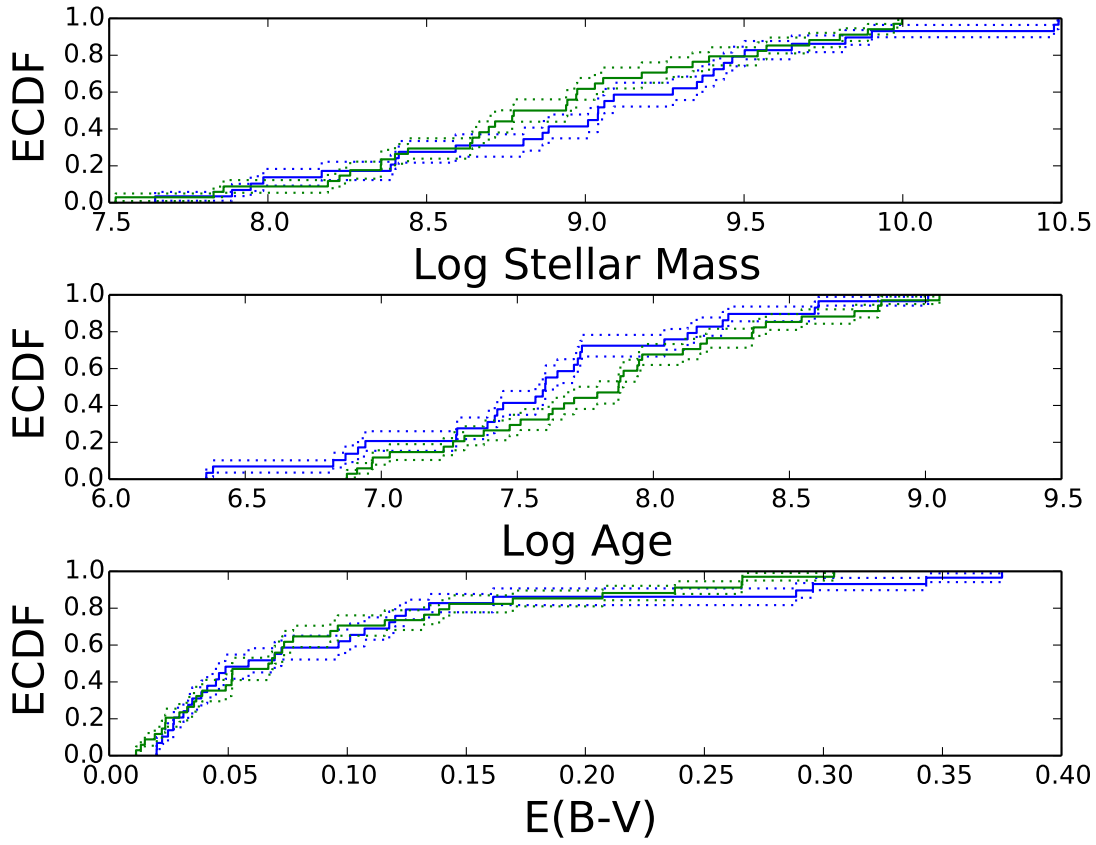

Fig. 2.— The Empirical Cumulative Distribution Functions of the clean sample of LAEs (blue), compared to those for LAEs with lower-probability counterparts (green). The dotted lines represent the $1\,\sigma$ asymtotic errors (Donsker 1952). In all cases the K-S test cannot reject the null hypothesis that both samples are drawn from the same underlying distribution.

These aperture magnitudes were then used to define each LAE's half-light radius. As described by Bond et al. (2012), the uncertainty in this type of measurement is given by

$$\frac{\sigma_r}{r} = 0.54\,\frac{\sigma_f}{f} \tag{1}$$

where r is the half-light radius, f and σ_f are the flux and associated flux uncertainty, and σ_r is the resultant error on the half-light radius. For our sample of LAEs as a whole, the fractional median uncertainty for the measured half-light radius is 4%. We note that this measure of size is much less sensitive to the $(1+z)^4$ effects of cosmological surface brightness dimming than estimates based on limiting isophotes. Furthermore, the observations differ in depth (COSMOS is a single orbit while GOODS is 2.5 orbits), and so any biases from surface brightness limits can be found by comparing the half-light radii from both surveys. A two-sample KS-test showed that the distributions of half-

light radii derived from GOODS and COSMOS are not significantly different and thus we should not be concerned about effects from cosmological surface brightness dimming.

4. Results

Table 3 gives the best-fit solutions to our SED fits, their reduced χ^2 values, and the LAE's half-light radii as measured on the *HST* frames. We discuss these results below.

4.1. Size

The left-hand panel of Figure 3 shows the distribution of half-light radii for the 63 luminous Lyα emitters in our sample.[4] From the figure, it is clear that the highly luminous LAEs of the HPS have a wide range of sizes: while the peak of the distribution is close to 1.2 kpc, there is a distinct tail that extends all the way out to $\sim$ 4 kpc. The median of the distribution is $1.35^{+0.08}_{-0.10}$ kpc, where the 68% confidence interval comes from a bootstrap analysis (Efron 1987). For comparison, the typical size of the narrow-band selected $2 < z < 3$ LAEs studied by Bond et al. (2012) is ~ 1.0 kpc, while that for $z \sim 3$ Lyman-break galaxies is close to 4 kpc (Pentericci et al. 2010). As demonstrated by Spearman rank correlation coefficient ($\rho = -0.15$) and Figure 4, these sizes show no significant correlation with redshift; this result is consistent with that of Malhotra et al. (2012), who also saw no size evolution in samples of narrow-band selected LAEs between $2.5 < z < 6$. This is in contrast with the strong evolution seen in the sizes of LBGs over the same redshift range (e.g. Ferguson et al. 2004).

On the other hand, as the right-hand panel of Figure 3 shows, there is a relation between LAE half-light radius, as measured in the rest-frame UV, and the amount of luminosity emitted in the Lyα line. Although the scatter in the diagram is substantial, the Spearman rank order coefficient reveals a positive correlation between the two variables ($\rho = +0.31$), which is significant at the $2.5\,\sigma$ (99%) level. Moreover, up to a half-light radius of 2.5 kpc, $\rho = +0.45$, implying a $3.4\,\sigma$ (99.9% confidence) result. Within this range, Lyα luminosity appears to grow linearly with galaxy size with a slope of $0.6 \pm 0.2 \times 10^{43}$ erg s^{-1} kpc^{-1}. Unfortunately, the data outside this range are too sparsely populated to draw any conclusions.

[4]This type of plot will be used throughout this work and shows a histogram, a kernel density estimation (KDE), and the empirical cumulative distribution function (ECDF). All KDEs contained herein use a Gaussian kernel and were calculated using the *density* function in R (R Core Team 2012). The bandwidth for each KDE was found using the rule of thumb from Scott (1992). A simple change in the choice of bins for a histogram can change the interpretation of the science; since KDEs do not require binning, they do not suffer from this effect. Every ECDF plotted will also have dotted upper and lower limits, which represent the 1σ asymptotic errors (Donsker 1952).

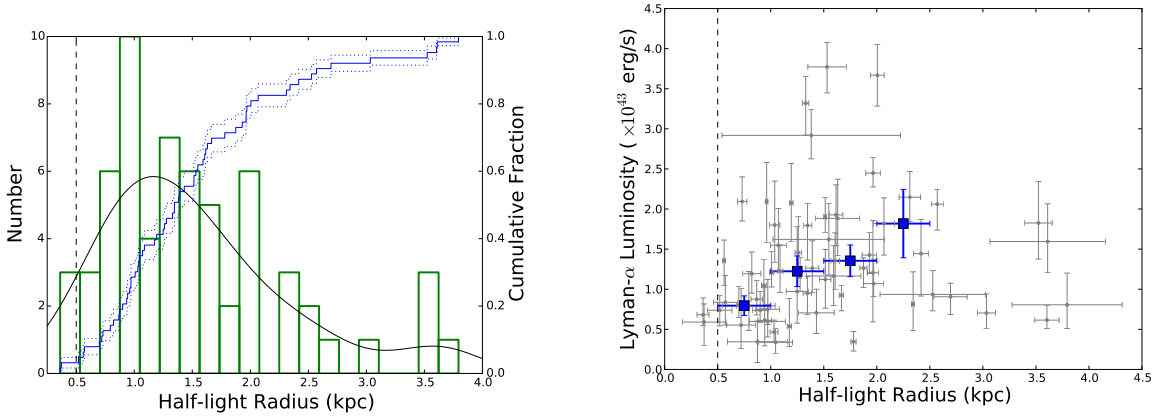

Fig. 3.— *Left:* A histogram showing the distribution of half-light radii for the HPS LAEs. The cumulative distribution is shown in blue, while the kernel density estimation (KDE) of the distribution is in black. The dashed line illustrates the resolution limit of the data. The median half-light radius of 1.35 kpc is consistent with that found for narrow-band selected LAEs at $z \sim 2.1$, but larger than the median at $z \sim 3.1$ (Bond et al. 2012). *Right:* A comparison of half-light radius to Lyα luminosity. The grey points are the individual measurements, while the dark blue squares show the median value of each bin. The error bars in x delineate the size of each bin, while the error bars in y report the bin's standard error. Although the scatter is large, the correlation for LAEs with $r < 2.5$ kpc is significant at the $3.4\,\sigma$ (99.9%) confidence level, and for the entire sample, the trend is confirmed with $2.5\,\sigma$ (99%) confidence.

4.2. Stellar Mass

At $2 < z < 3$, SED stacking analyses have produced estimates for the median LAE mass in the range of $\sim 10^8$ to $10^{10} M_\odot$, depending on whether the samples under study were detectable on Spitzer/IRAC images (Lai et al. 2008; Guaita et al. 2011; Acquaviva et al. 2011). In the left-hand panel of Figure 5, we show the distribution of *individual* LAE masses derived from our constant star formation rate model. Although the median mass of $\log(M/M_\odot) = 8.97^{+0.06}_{-0.17}$ lies in the range inferred from the previous stacking analyses, the data span a factor of a thousand, from $M \sim 10^{7.5}$ to $10^{10.5}\,M_\odot$. This distribution is consistent with that recently found by McLinden et al. (2014) for a set of extremely luminous ($L(\mathrm{Ly}\alpha) > 10^{43}$ ergs s^{-1}) $z \sim 3.1$ LAEs found via narrow-band imaging. Interestingly if we fit our LAE mass distribution with a power law over the range $8.5 < \log M/M_\odot < 10.5$, then the most-likely slope, $\alpha = -1.3 \pm 0.1$, is similar, or perhaps only slightly shallower than the slope usually adopted for the epoch's galaxy mass function (e.g., Muzzin et al. 2013; Tomczak et al. 2013). This suggests that bright Lyα emitters are drawn from an underlying distribution that is not strongly dependent on stellar mass. Moreover, as the right-hand panel of Figure 5 demonstrates, there is no obvious correlation between stellar mass and Lyα luminosity: at any $\log L$, one can find LAEs of all masses, and galaxies of any given mass can have a wide range of Lyα luminosity. Unless this behavior abruptly changes at low Lyα luminosity, it

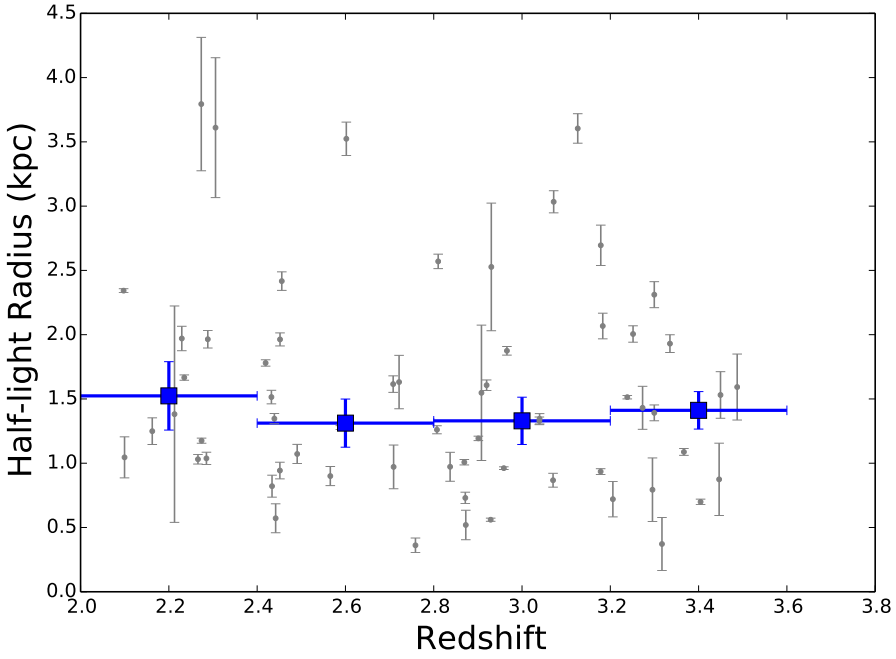

Fig. 4.— The lack of LAE size evolution with redshift. The grey points are individual measurements while the blue squares are binned medians. A bias in size measurement from cosmic surface brightness dimming would manifest as a decrease in half-light radius as $(1+z)^4$. There is no evidence for this effect.

would appear that large-volume LAE surveys are an excellent way of sampling virtually the entire range of the high-redshift galaxy mass function.

One additional feature of Figure 5 worth noting is the absence of LAEs with masses less than $\sim 5 \times 10^7 M_\odot$. There are two possible reasons for this. The first is the depth of the imaging: there are seven sources in the HPS survey for which Adams et al. (2011) could find no obvious counterpart in the rest-frame UV. An examination of the CANDELS frames and grism spectra from the 3D-HST program (van Dokkum et al. 2013) reveals that only one of these missing objects has any detectable flux in the rest-frame optical. (The counterpart of HPS 266 is detected at $\alpha(2000)$ =10:00:29.818, $\delta(2000)$ =+2:18:49.20.) The missing 6 objects may therefore be part of the extreme low-mass tail of the mass function.

A second possible explanation for the missing lower-mass galaxies comes from the limitations imposed by our input physics. Formally, the population synthesis models of Bruzual & Charlot (2003) are applicable to stellar systems with ages between $10^5 < t < 2\times10^{10}$ yr. However, the CB07 (and BC03) models used in our analysis, and the Padova isochrones upon which they are based, were developed using stars with ages of $10^{6.6}$ years and older (Conroy 2013). Any system younger than this must therefore be subject to greater systematic uncertainties. The lack of systems with

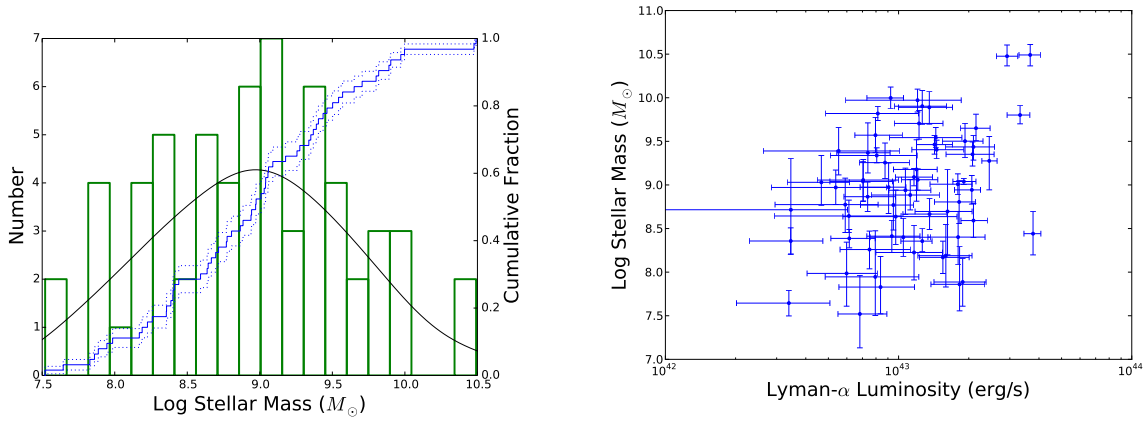

Fig. 5.— *Left:* The distribution of masses for the HPS LAEs under the assumption of a constant star formation rate throughout history. The items plotted on the left figure are described in the caption of Figure 3. The distribution is very nearly flat in the log over 3 orders of magnitude. *Right:* a comparison of galaxy mass with Lyα luminosity. There is no significant correlation between the two parameters, implying that the sample's Lyα flux-limit does not propagate strongly into a constraint on stellar mass.

masses below $\sim 5 \times 10^7 M_\odot$ may therefore be an artifact of our SED fitting. Furthermore, since our SED fits assume a constant star formation rate, very low mass systems almost certainly have very young ages, further increasing the potential for systematic errors at the very faint end of our sample.

Figure 6 plots our derived stellar masses against two parameters, LAE size and redshift. Neither shows a significant trend. While Bond et al. (2012) did find a correlation between mass and half-light radius, their analysis dealt with stacked images, not individual SEDs. Our null result also agrees with that found for surveys of UV-bright galaxies in the same redshift range. LAE sizes (as measured in the UV continuum) and stellar masses do not seem to be related (e.g., Mosleh et al. 2011).

4.3. $E(B-V)$

Since Lyα photons resonantly scatter off interstellar hydrogen, even a small amount of extinction can reduce the emergent emission-line flux by several orders of magnitude. Thus, it has long been argued that LAEs are mostly young, metal-poor objects with very little dust (e.g., Gawiser et al. 2006; Mao et al. 2007). Nevertheless, evidence for the existence of dust within LAEs has been seen in the work of Finkelstein et al. (2009) among others. As the left-hand panel of Figure 7 illustrates, our data demonstrate that, indeed, most LAEs are dust-poor. Based on our SED analyses, half of the HPS LAEs have internal stellar reddenings $E(B-V) < 0.07$, though there is a

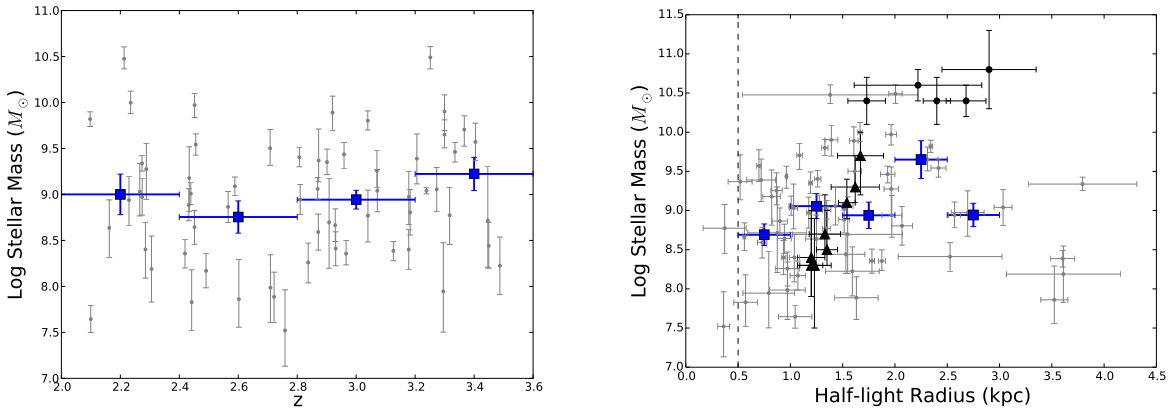

Fig. 6.— The left panel displays stellar masses versus redshift, with the individual LAEs shown in grey and the median values for each redshift bin plotted as blue squares. The right panel similarly compares stellar mass to half-light radius. The dashed line illustrates the limit of our spatial resolution. In both figures, the error bars in x illustrate the sizes of the bins, while the errors in y report the standard error within each bin. The black circles are averages of various continuum selected galaxies from Mosleh et al. (2011) and the black triangles are results from stacks by Bond et al. (2012).

tail that extends all the way out to $E(B-V) \sim 0.4$. The median of the $E(B-V)$ distribution is $0.067^{+0.003}_{-0.018}$. Notably, all the high-extinction objects are drawn from the high-mass end of the LAE mass function: every LAE with $E(B-V) > 0.25$ has a mass greater than $\sim 10^9 M_\odot$. This agrees with correlations between mass and extinction seen in both the local universe and at high redshift (e.g., Garn & Best 2010; Kashino et al. 2013).

Figure 8 displays our estimates of differential reddening versus redshift and galaxy size. There are no significant trends in either diagram. Unlike Guaita et al. (2011) and Acquaviva et al. (2011), we see no evidence for any change in the mean reddening of the LAE population versus redshift, and, unlike Bond et al. (2012), we see no correlation between $E(B-V)$ and half-light radius. Again, we caution that the LAE samples considered here are more luminous than those derived from narrow-band surveys, and by studying individual, rather than stacked spectra, we are avoiding many of the systematic difficulties that complicate the interpretation of previous measurements (Vargas et al. 2014).

4.4. Age

Figure 9 displays the age distribution for the HPS LAEs, under the simplest assumption of a constant star-formation rate history. The two figures together support the stacking analyses of Lai et al. (2008), Guaita et al. (2011), and Acquaviva et al. (2011), which argued that LAEs are

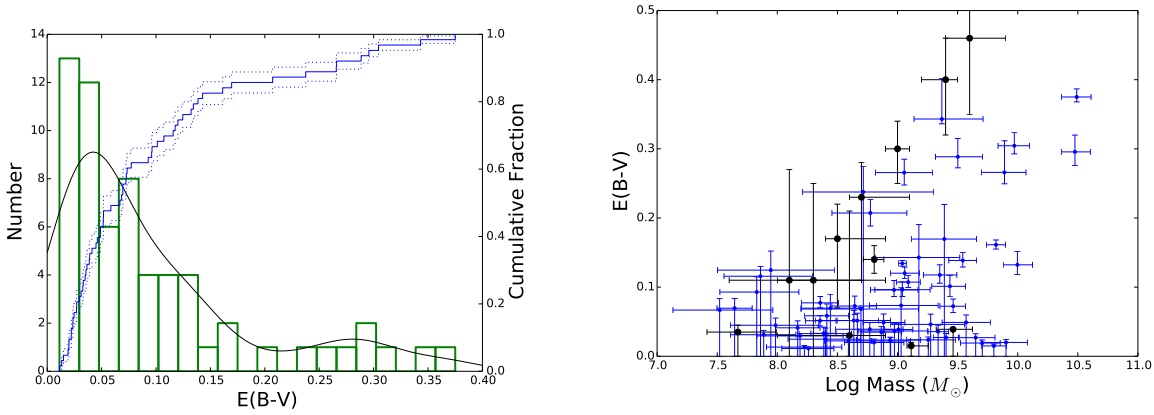

Fig. 7.— *Left:* The distribution of stellar reddenings derived from our constant SFR models. The items plotted are described in the caption of Figure 3. The median of the distribution is $E(B-V) = 0.07$, but there is a tail that extends out to $E(B-V) \sim 0.4$. *Right:* The stellar reddening of our LAEs as a function of galaxy mass. The black circles represent the results of stacking analyses for LAEs at $z \sim 2.1$ and $z \sim 3.1$ (Acquaviva et al. 2011; Acquaviva et al. 2012; Guaita et al. 2011). Low mass objects are uniformly dust-poor, but objects with $M > 10^9\,M_\odot$ can have a wide range of internal extinction. Stellar mass and extinction are correlated with a Spearman rank coefficient of $\rho = 0.3$, indicating $2.4\,\sigma$ (98.5%) significance.

relatively young, with ages between $\sim 10^7$ and 10^9 years. The median age of the HPS sample is $\log t = 7.96^{+0.19}_{-0.14}$, and just $\sim 3\%$ have ages greater than a Gyr. Interestingly, there no evidence for evolution in the sample. This disagrees with result of Guaita et al. (2011), who found narrow-band selected $z = 2.06$ LAEs to be older and dustier than their $z = 3.1$ counterparts. It is also in conflict with the re-analysis by Acquaviva et al. (2012), who concluded that these same LAEs were "growing younger" with time. A likely explanation for this discrepancy lies in the details of the stacking procedure used by both groups, as slight differences can produce discrepant results (see Vargas et al. 2014). Our analysis of individual LAEs avoids that pitfall.

4.5. Star Formation Rates and the Main Sequence of Galaxies

The observed star formation rate of an LAE can be derived several ways: from the luminosity of its Lyα emission line via the assumption of Case B recombination,

$$\mathrm{SFR(Ly}\alpha) = 9.1 \times 10^{-43}\,L(\mathrm{Ly}\alpha)\ M_\odot\ \mathrm{yr}^{-1} \tag{2}$$

(Brocklehurst 1971; Kennicutt 1998), from the extinction-corrected flux density of the UV continuum between 1500 Å and 2800 Å

$$\mathrm{SFR(UV)} = 1.4 \times 10^{-28}\,L_\nu\ M_\odot\ \mathrm{yr}^{-1} \tag{3}$$

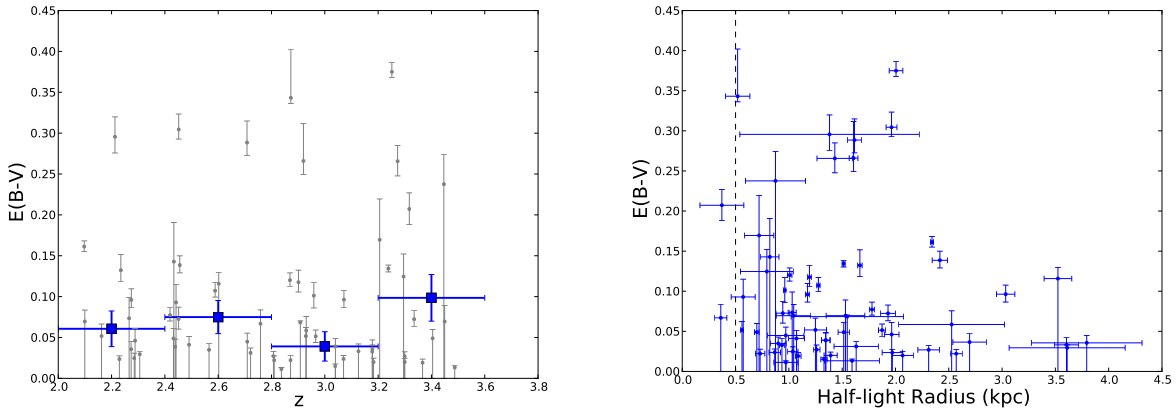

Fig. 8.— Comparisons of stellar reddening with redshift (left) and half-light radius (right). The grey points show individual LAEs while the blue points illustrate the median values within each bin. The dashed line shows the limit of our spatial resolution. Neither diagram displays a significant trend.

(Kennicutt 1998), and via the fit to the object's spectral energy distribution (a value which is largely dependent on the UV emission, but which may also include factors such as age).

Figure 10 plots our dust-corrected UV SFRs against stellar mass, and compares these data to those obtained from other samples of high-z galaxies. From the figure, it is clear that each selection technique identifies galaxies in a different region of the mass-SFR diagram. LAEs are primary low-mass, low-SFR objects that lie above the star-forming main sequence found by Daddi et al. (2007), in a region of the diagram consistent with measurements of galaxy main-sequence evolution (Whitaker et al. 2012). Both IFU and narrow-band selected LAEs fall in this same region, confirming that both discovery techniques trace the same population. UV continuum-detected (BzK) galaxies are higher-mass, high-SFR objects, while *Herschel*-PACS-selected sub-mm galaxies are high-mass objects that, like LAEs, fall predominantly above the star-forming main sequence (Rodighiero et al. 2011). As the distributions of LAEs and sub-mm galaxies abut each other, it is tempting to associate the two classes. If sub-mm systems are the results of merger-driven starbursts (Conselice et al. 2003), then LAEs could potentially be their low mass and low-dust counterparts: in general, a starburst event will move a galaxy up and slightly to the right on this diagram. Gronwall et al. (2011), however, see no strong evidence for interactions in LAE morphologies.

4.6. Lyα Escape Fractions and the q-factor

Like the UV flux density, the Hα emission line is a well-known and well-understood star formation rate indicator (Kennicutt 1998). Since under Case B recombination, roughly three quarters of all Balmer transitions produce a Lyα photon, this means that Lyα should also be a robust tracer

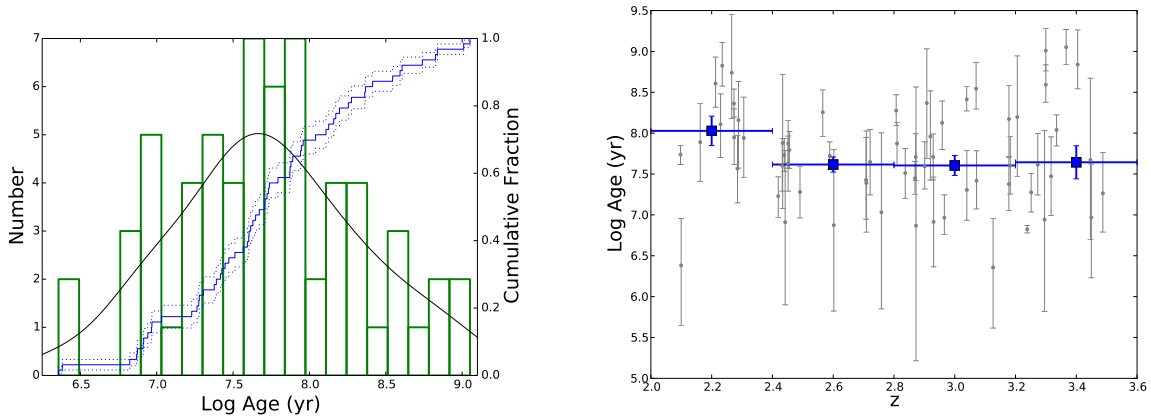

Fig. 9.— *Left:* The age distribution of the HPS LAEs. The ages extend over ~ 2.5 dex. *Right:* The distribution of LAE ages versus redshift, with individual objects plotted in grey and binned medians in blue. There is no evidence for evolution in the LAE population.

of star formation. Thus, *if* all the Lyα and UV continuum photons escape into intergalactic space, Lyα and the dust-corrected UV continuum should be well-correlated. Systematic deviations from a one-to-one relation then measure the escape fraction of Lyα photons. Note that this differential procedure sidesteps the issue of whether the reddening derived from the stars is the same as that for the gas, but it does assume that both the UV and Lyα emission is isotropic. It is also susceptible to a systematic error associated with the timescale of star formation. The nominal conversion between UV emission and star formation rate (equation 3) assumes a timescale for star formation that is ten times longer than that for emission line gas. If a system is undergoing a rapid burst of star formation ($\tau < 10^8$ yr), its two SFRs indicators may not be comparable. Nevertheless, the ratio of UV flux to Lyα can provide constraints on the radiative transfer of the emission line.

The question of the dependence of Lyα escape fraction on SFR and redshift has been recently discussed in Dijkstra & Jeeson-Daniel (2013). This paper presents two models: one in which the escape fraction is independent of star formation rate, and a second where the escape fraction decreases as the SFR increases. We find a significant inverse correlation between stellar mass and escape fraction, $\rho = -0.54$ ($4.5\,\sigma$ or $> 99.999\%$ significance) which supports the second model; this is shown in Figure 12. Unsurprisingly, the Lyα escape fraction also correlates with differential extinction, as mass and $E(B-V)$ are coupled (see Fig. 7). We note that the median escape fraction of our sample, ~ 0.5 (or 0.6, if we use the SED-based SFRs), is somewhat larger than the 0.29 value found by Blanc et al. (2011) using the same sample of LAEs. Most of this difference is due to the use of deeper CANDELS data, which greatly improves the photometry and fixes the slope of the rest-frame UV.

Perhaps a more useful way of looking at the radiative transfer problem is through the variable q, which relates Lyα optical depth to that of the stellar continuum at 1216 Å. As defined by

Finkelstein et al. (2008),

$$q = \frac{\tau_{Ly\alpha}}{\tau_{1216}} \tag{4}$$

where $\tau_\lambda = 0.921\, k_\lambda E(B-V)$ and $k_{1216} = 5.27$ under the empirical reddening law described by Calzetti (2001). Figure 11 shows the distribution of q values and the behavior of q with $E(B-V)$. Interestingly, at large reddenings q never gets much above 1, suggesting that in these systems, the Lyα emitting gas and the UV starlight are seeing the same amount of extinction. We do expect that galaxies with large Lyα optical depths will be censored out of our LAE sample. However, in dust-rich systems it appears that, if Lyα escapes, it does so with very few resonant scatterings. This is consistent with models that involve strong winds, such as that proposed by Verhamme et al. (2008). On the other hand, at low reddenings, we see a large range of q values. Systems with $q < 0$ imply anisotropic emission, a top-heavy IMF, or a very young starburst, where the UV luminosity to SFR conversion breaks down. As expected, we find that the half-light radius and q-factor are positively correlated, with a Spearman rank order coefficient of $\rho = 0.35$ (99.5% confidence). This correlation is shown in the right hand panel of Figure 12. A small size could lead to less homogeneity and thus more opportunities for Lyα to undergo anisotropic radiative transfer.

5. Conclusion

Using broadband photometric data which extends from the rest-frame UV through to the near-IR, we have been able to measure the stellar masses, reddenings, and sizes for a sample of 63 luminous LAEs found in the HETDEX Pilot Survey. Our fits demonstrate that, contrary to popular belief, Lyα emitters are not exclusively low mass objects. In fact, HPS-selected LAEs are quite heterogeneous, and are drawn from almost the entire stellar mass range of high-redshift galaxies. Moreover, there is a striking similarity between the mass function of LAEs and the mass function expected for the galactic star-forming population as a whole. This fact, and the lack of correlation between Lyα luminosity and stellar mass, suggests that searches for Lyα emission are excellent way of sampling a large fraction of the mass function of high-redshift star-forming galaxies.

Lyα-emitting galaxies occupy a different part of stellar mass-SFR parameter space than that of galaxies found by other methods. Like the higher-mass sub-mm galaxies, LAEs fall above the main sequence of star-forming galaxies found by Daddi et al. (2007). This suggests that there is a different slope for the main sequence of star-bursting galaxies. Interestingly, LAEs do fall along the main sequence defined by Whitaker et al. (2012), though the ~ 2 dex extrapolation required to reach their masses introduces significant uncertainty. Due to the various selection effects at work, the connection between the various classes of star-forming galaxies is murky at best.

We also find that the range in observed q-factors is dependent on the reddening, with the widest range of q-values occurring at low extinction. Interestingly, the observed values of q tend to unity as the reddening (or mass) increases, suggesting that in these objects, Lyα photons are not undergoing a large number of scattering events. This strongly implies that winds are an important

component in the making of high-mass LAEs. Furthermore, we find that the half-light radius and the q-factor are positively correlated, implying that Lyα emission is enhanced in very small objects.

Acknowledgments

We thank the referee for their helpful comments. We also thank Joshua Adams for the use of his photometry from the HETDEX Pilot Survey. We acknowledge the Research Computer and Cyberinfrastructure Unit of Information Technology Services, and in particular W. Brouwer at The Pennsylvania State University for providing computational support and resources for this project. This work is based on observations taken by the CANDELS Multi-Cycle Treasury Program with the NASA/ESA HST, which is operated by the Association of Universities for Research in Astronomy, Inc., under NASA contract NAS5-26555. The work was also partially supported by NSF grants AST 09-26641 and AST 10-55919. The Institute for Gravitation and the Cosmos is supported by the Eberly College of Science and the Office of the Senior Vice President for Research at the Pennsylvania State University.

This research has made use of NASA's Astrophysics Data System and the python packages `IPython`, `NumPy`, `SciPy`, and `matplotlib`.

Facilities: CFHT, HST, Mayall Smith, Spitzer (IRAC), Subaru, UH:2.2m, UKIRT

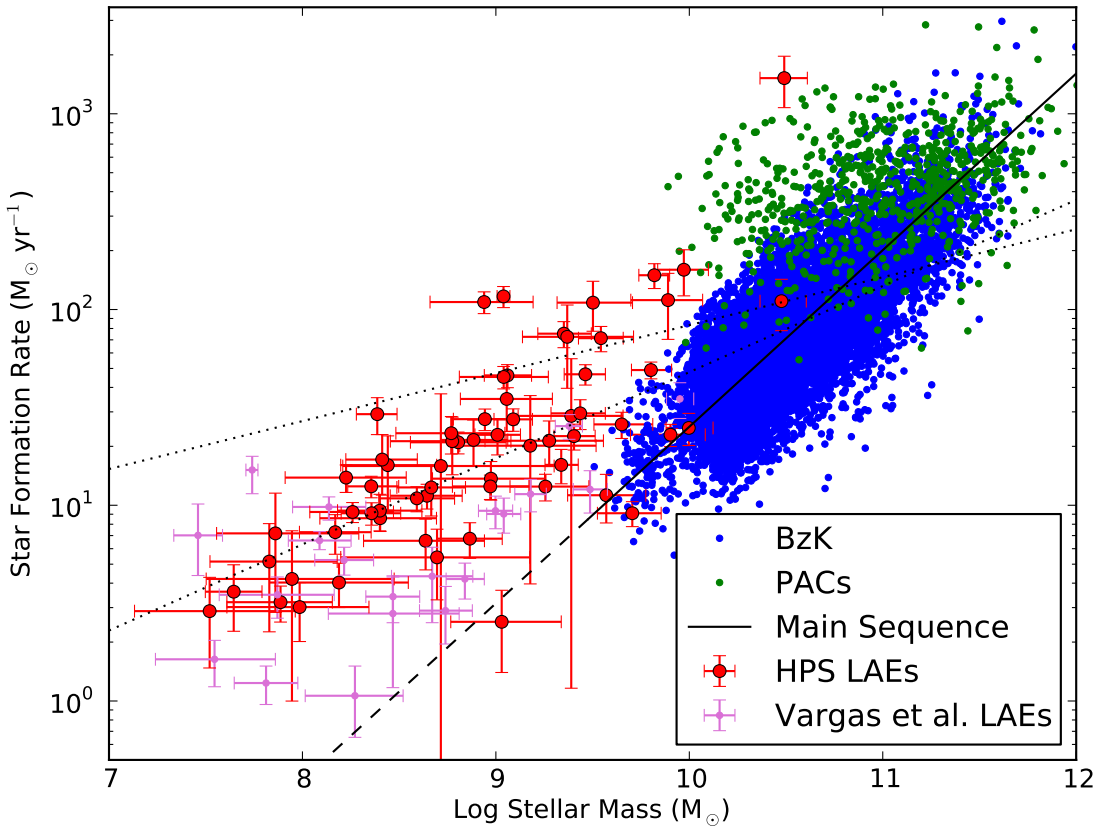

Fig. 10.— Dust corrected UV star formation rate plotted against stellar mass for various high-redshift galaxies. Our luminous, spectroscopically-selected LAEs are shown in red, and narrow-band selected LAEs from Vargas et al. (2014) are in pink. The blue and green points show higher-mass galaxies from the Rodighiero et al. (2011) survey of COSMOS and GOODS-N: blue are continuum-selected (BzK) galaxies, while green shows sub-mm bright systems found by the *Herschel*-PACS instrument. The solid black line is the star-forming "main sequence" defined by Daddi et al. (2007) for $1.5 < z < 2.5$; the extrapolation of this line to lower SFRs is shown with a dashed line. LAEs and sub-mm galaxies lie above this relation, along the main sequences found by Whitaker et al. (2012) for $z = 2.0$ (lower dotted line) and $z = 3.5$ (upper dotted line).

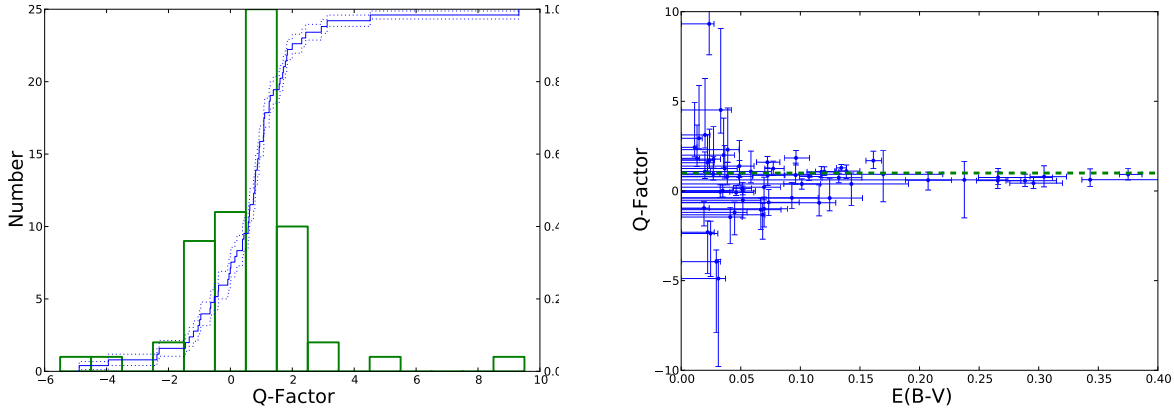

Fig. 11.— *Left:* A histogram of the q-parameters for our spectroscopically selected LAEs. *Right:* These same q values as a function of $E(B-V)$. The data are biased, in that systems with large values of q will have Lyα suppressed below the limit of detectability. All dusty systems have q near 1, while systems with small $E(B-V)$ can have a range of q values.

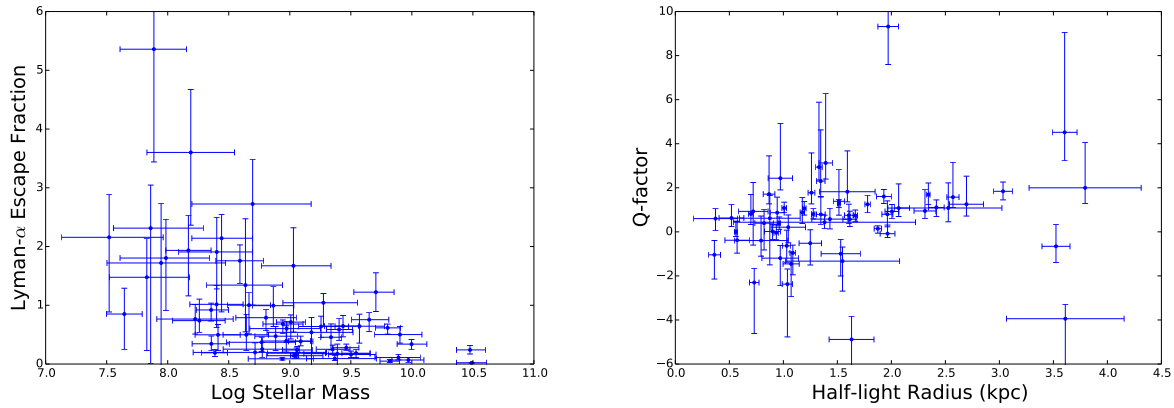

Fig. 12.— *Left:* The escape fraction of Lyα photons as a function of stellar mass. Note the negative correlation. Values greater than one can be due to an anisotropic ISM, as Lyα may be escaping through voids blown out by supernovae or other feedback. The decline in the maximum escape fraction with stellar mass supports this model, as it would take much more energy to blow out a hole in a massive galaxy. *Right:* The correlation between half-light radius and q; galaxies with small or negative q factors are physically smaller. This is again consistent with the idea with anisotropic Lyα emission, as it would be easier for supernovae to create holes in smaller, less massive galaxies.

REFERENCES

Acquaviva, V., Gawiser, E., & Guaita, L. 2011, ApJ, 737, 47

Acquavivia, V. 2012, private communication

Acquaviva, V., Vargas, C., Gawiser, E., & Guaita, L. 2012, ApJ, 751, L26

Adams, J.J., Blanc, G.A., Hill, G.J., et al. 2011, ApJS, 192, 5

Atek, H., Siana, B., Scarlata, C., et al. 2011, ApJ, 743, 121

Bell, E.F., & de Jong, R.S. 2001, ApJ, 550, 212

Bertin, E., & Arnouts, S. 1996, A&AS, 117, 393

Blanc, G.A., Adams, J.J., Gebhardt, K., et al. 2011, ApJ, 736, 31

Brocklehurst, M. 1971, MNRAS, 153, 471

Bond, N.A., Gawiser, E., Gronwall, C., et al. 2009, ApJ, 705, 639

Bond, N.A., Gawiser, E., Guaita, L., et al. 2012, ApJ, 753, 95

Brooks, S., & Gelman, A. 1998, J. of Comp. & Graph. Stat., 7, 434

Bruzual, G., & Charlot, S. 2003, MNRAS, 344, 1000

Calzetti, D. 2001, PASP, 113, 1449

Capak, P., Aussel, H., Ajiki, M., et al. 2007, ApJS, 172, 99

Chabrier, G. 2003, PASP, 115, 763

Chonis, T.S., Blanc, G.A., Hill, G.J., et al. 2013, ApJ, 775, 99

Conroy, C. 2013, ARA&A, 51, 393

Conselice, C. J., Chapman, S. C., & Windhorst, R. A. 2003, ApJ, 596, L5

Cowie, L.L., & Hu, E.M. 1998, ApJ, 115, 1319

Cowie, L.L., Barger, A.J., & Hu, E.M. 2010, ApJ, 711, 928

Daddi, E., Dickinson, M., Morrison, G., et al. 2007, ApJ, 670, 156

Deharveng, J.M., Small, T., Barlow, T.A., et al. 2008, ApJ, 680, 1072

Dijkstra, M. & Jeeson-Daniel, A. 2013, MNRAS, 435, 3333

Donsker, M. 1952, Ann. Math. Statist., 23, 393

Drory, N., Feulner, G., Bender, R., et al. 2001, MNRAS, 325, 550

Efron, B. 1987, J. Amer. Stat. Assoc., 397, 171

Ferguson, H.C. et al. 2004, ApJ, 600, 107

Finkelstein, S.L., Rhoads, J.E., Malhotra, S., Grogin, N., & Wang, J. 2008, ApJ, 678, 655

Finkelstein, S.L., Rhoads, J.E., Malhotra, S., & Grogin, N. 2009, ApJ, 691, 465

Finkelstein, S.L., Hill, G.J., Gebhardt, K., et al. 2011, ApJ, 729, 140

Finkelstein, S.L., Papovich, C., Dickinson, M., et al. 2013, Nature, 502, 524

Garn, T., & Best, P. N. 2010, MNRAS, 409, 421

Gawiser, E., van Dokkum, P.G., Gronwall, C., et al. 2006, ApJ, 642, L13

Gawiser, E., Francke, H., Lai, K., et al. 2007, ApJ, 671, 278

Gelman, A. & Rubin, D. 1992, Stat. Sci., 7, 457

Giavalisco, M., Ferguson, H.C., Koekemoer, A.M., et al. 2004, ApJ, 600, L93

Gronwall, C., Ciardullo, R., Hickey, T., et al. 2007, ApJ, 667, 79

Gronwall, C., Bond, N.A., Ciardullo, R., et al. 2011, ApJ, 743, 9

Grogin, N.A., Kocevski, D.D., Faber, S.M., et al. 2011, ApJS, 197, 35

Guaita, L., Gawiser, E., Padilla, N., et al. 2010, ApJ, 714, 255

Guaita, L., Acquaviva, V., Padilla, N., et al. 2011, ApJ, 733, 114

Hill, G.J., MacQueen, P.J., Smith, M.P., et al. 2008, Proc. SPIE, 7014, 231

Hinshaw, G., Larson, D., Komatsu, E., et al. 2013, ApJS, 208, 19

Hu, E.M., Cowie, L.L., & McMahon, R.G. 1998, ApJ, 502, L99

Hu, E.M., Cowie, L.L., Barger, A.J., et al. 2010, ApJ, 725, 394

Kashino, D., Silverman, J. D., Rodighiero, G., et al. 2013, ApJ, 777, L8

Kauffmann, G., Heckman, T.M., White, S.D.M., et al. 2003, MNRAS, 341, 33

Kennicutt, R. 1998, ARA&A, 36, 189

Koekemoer, A.M., Faber, S.M., Ferguson, H.C., et al. 2011, ApJS, 197, 36

Kroupa, P. 2001, MNRAS, 322, 231

Lai, K., Huang, J.-S., Fazio, G., et al. 2008, ApJ, 674, 70

Lewis, A., & Bridle, S. 2002, Phys. Rev. D, 66, 103511

Lidman, C., Hayes, M., Jones, D.H., et al. 2012, MNRAS, 420, 1946

Madau, P. 1995, ApJ, 441, 18

Makovoz, D., & Marleau, F. 2005, PASP, 117, 1113

Malhotra, S., Rhoads, J.E., Finkelstein, S.L., et al. 2012, ApJ, 750, L36

Mannucci, F., Cresci, G., Maiolino, R., Marconi, A., & Gnerucci, A. 2010, MNRAS, 408, 2115

Mao, J., Lapi, A., Granato, G.L., de Zotti, G., & Danese, L. 2007, ApJ, 667, 655

McLinden, E.M., Rhoads, J.E., Malhotra, S., et al. 2014, MNRAS, in press (arXiv: 1402.5227)

Mosleh, M., Williams, R.J., Franx, M., & Kriek, M. 2011, ApJ, 727, 5

Muzzin, A., Marchesini, D., Stefanon, M., et al. 2013, ApJ, 777, 18

Nakajima, K., Ouchi, M., Shimasaku, K., et al. 2012, ApJ, 745, 12

Nakajima, K., Ouchi, M., Shimasaku, K., et al. 2013, ApJ, 769, 3

Nilsson, K.K., Östlin, G., Möller, P., et al. 2011, A&A, 529, A9

Ono, Y., Ouchi, M., Mobasher, B., et al. 2012, ApJ, 744, 83

Ouchi, M., Shimasaku, K., Akiyama, M., et al. 2008, ApJS, 176, 301

Ouchi, M., Shimasaku, K., Furusawa, H., et al. 2010, ApJ, 723, 869

Papovich, C., Finkelstein, S.L., Ferguson, H.C., Lotz, J.M., & Giavalisco, M. 2011, MNRAS, 412, 1123

Partridge, R., & Peebles, P.J. 1967, ApJ, 147, 868

Pentericci, L., Grazian, A., Scarlata, C., et al. 2010, A&A, 514, A64

Pierre, M., Valtchanov, I., Altieri, B., et al. 2004, J. Cosmology Astropart. Phys., 9, 11

Planck Collaboration: Ade, P.A.R., Aghanim, N., Armitage-Caplan, C., et al. 2013, submitted to A&A(arXiv:1303.5076)

R Core Team 2012, R: A Language and Environment for Statistical Computing. `http://www.R-project.org/`

Rodighiero, G., Daddi, E., Baronchelli, I., et al. 2011, ApJ, 739, L40

Salpeter, E. 1955, ApJ, 121, 161

Scott, D. 1992, Multivariate Density Estimation: Theory, Practice, and Visualization, (New York: Wiley)

Scoville, N., Aussel, H., Brusa, M., et al. 2007, ApJS, 172, 1

Shapley, A.E., Steidel, C.C., Pettini, M., & Adelberger, K.L. 2003, ApJ, 588, 65

Schaerer, D., & de Barros, S. A&A, 502, 423

Song, M., Finkelstein, S.L., Gebhardt, K., et al. 2013, submitted to ApJ

Tomczak, A.R., Quadri, R.F., Tran, K.-V.H., et al. 2013, ApJ, in press (arXiv:1309.5972)

van Dokkum, P., Brammer, G., Momcheva, I., et al. 2013, arXiv:1305.2140

Vargas, C.J., Bish, H., Acquaviva, V., et al. 2014, ApJ, 783, 26

Verhamme, A., Schaerer, D., Atek, H., & Tapken, C. 2008, A&A, 491, 89

Verhamme, A., Dubois, Y., Blaizot, J., et al. 2012, A&A, 546, A111

Whitaker, K.E., van Dokkum, P.G., Brammer, G., & Franx, M. 2012, ApJ, 754, L29

Yuma, S., et al. 2010, ApJ, 720, 1016

Zibetti, S., Charlot, S., & Rix, H.-W. 2009, MNRAS, 400, 1181

This preprint was prepared with the AAS LaTeX macros v5.2.

Table 1. COSMOS Field Photometry

Telescope	Instrument	Filter	Central λ (Å)	Original Survey	Photometry	5σ Limits (AB)
CFHT	Megaprime	u*	4065	COSMOS	Adams et al. (2011)	26.5
Subaru	Suprime-Cam	B	4788	COSMOS	Adams et al. (2011)	27.4
Subaru	Suprime-Cam	V	5730	COSMOS	Adams et al. (2011)	27.2
Subaru	Suprime-Cam	r+	6600	COSMOS	Adams et al. (2011)	26.9
HST	ACS	F814W	7461	CANDELS	Song et al. (2013)	27.5
Subaru	Suprime-Cam	i+	7850	COSMOS	Adams et al. (2011)	26.9
Subaru	Suprime-Cam	z+	8700	COSMOS	Adams et al. (2011)	25.6
UKIRT	WFCAM	J	12850	COSMOS	Adams et al. (2011)	23.6
HST	WFC3	F125W	13250	CANDELS	Song et al. (2013)	26.4
HST	WFC3	F160W	14460	CANDELS	Song et al. (2013)	26.5
CFHT	WIRCAM	K	21400	COSMOS	Adams et al. (2011)	23.6
Spitzer	IRAC	Channel 1	37440	S-COSMOS	This paper	23.9
Spitzer	IRAC	Channel 2	44510	S-COSMOS	This paper	23.3
Spitzer	IRAC	Channel 3	59950	S-COSMOS	This paper	21.3
Spitzer	IRAC	Channel 4	84870	S-COSMOS	This paper	21.0

Note. — CANDELS covers 32 of 42 objects in this field

Table 2. GOODS-N Field Photometry

Telescope	Instrument	Filter	Central λ (Å)	Original Survey	Photometry	5σ Limits (AB)
Mayall	MOSAIC	U	4065	GOODS	Adams et al. (2011)	27.1
HST	ACS	F435W	4570	CANDELS	Finkelstein et al. (2013)	27.8
Subaru	Suprime-Cam	B	4788	GOODS	Adams et al. (2011)	26.9
Subaru	Suprime-Cam	V	5730	GOODS	Adams et al. (2011)	26.8
Subaru	Suprime-Cam	r+	6600	GOODS	Adams et al. (2011)	26.6
HST	ACS	F606W	6690	CANDELS	Finkelstein et al. (2013)	27.6
HST	ACS	F775W	7380	CANDELS	Finkelstein et al. (2013)	27.5
Subaru	Suprime-Cam	i+	7850	GOODS	Adams et al. (2011)	25.6
HST	ACS	F850LP	8610	CANDELS	Finkelstein et al. (2013)	27.3
Subaru	Suprime-Cam	z+	8700	GOODS	Adams et al. (2011)	25.4
HST	WFC3	F105W	11783	CANDELS	Finkelstein et al. (2013)	26.6
HST	WFC3	F125W	13250	CANDELS	Finkelstein et al. (2013)	26.4
HST	WFC3	F160W	14460	CANDELS	Finkelstein et al. (2013)	26.5
UH 2.2-m	QUIRC	H+K'	20200	GOODS	Adams et al. (2011)	22.1
Spitzer	IRAC	Channel 1	37440	GOODS	This paper	23.9
Spitzer	IRAC	Channel 2	44510	GOODS	This paper	23.3
Spitzer	IRAC	Channel 3	59950	GOODS	This paper	21.3
Spitzer	IRAC	Channel 4	84870	GOODS	This paper	21.0

Note. — CANDELS covers 17 of 21 objects in this field

Table 3. SED Fitting Results

Galaxy ID	Redshift	Log Stellar Mass ($M_\odot$)	Log Age (yr)	$E(B-V)$	Half-light Radius (kpc)	χ^2_ν
HPS150	2.90	$9.35^{+0.14}_{-0.13}$	$7.59^{+0.30}_{-0.28}$	$0.118^{+0.015}_{-0.012}$	1.19 ± 0.02	4.1
HPS153	2.71	$9.50^{+0.20}_{-0.19}$	$7.43^{+0.52}_{-0.48}$	$0.289^{+0.026}_{-0.016}$	1.62 ± 0.06	1.5
HPS154	2.87	$9.37^{+0.34}_{-0.23}$	$6.87^{+1.70}_{-1.65}$	$0.343^{+0.059}_{-0.007}$	0.52 ± 0.11	3.5
HPS161	3.25	$10.49^{+0.12}_{-0.13}$	$7.28^{+0.23}_{-0.24}$	$0.375^{+0.012}_{-0.007}$	2.01 ± 0.06	1.0
HPS164	2.45	$9.97^{+0.13}_{-0.14}$	$7.87^{+0.28}_{-0.30}$	$0.304^{+0.019}_{-0.012}$	1.96 ± 0.05	2.9
HPS168	3.45	$8.44^{+0.25}_{-0.24}$	$6.97^{+0.65}_{-0.74}$	$0.070^{+0.020}_{-0.070}$	1.53 ± 0.18	2.8
HPS174	3.45	$8.72^{+0.59}_{-0.51}$	$7.67^{+1.00}_{-0.98}$	$0.238^{+0.037}_{-0.238}$	0.87 ± 0.28	3.2
HPS182	2.43	$9.18^{+0.34}_{-0.36}$	$7.88^{+0.84}_{-0.80}$	$0.143^{+0.048}_{-0.143}$	0.82 ± 0.09	5.0
HPS183	2.16	$8.64^{+0.30}_{-0.32}$	$7.89^{+0.47}_{-0.48}$	$0.052^{+0.015}_{-0.052}$	1.25 ± 0.10	2.3
HPS184	3.21	$9.39^{+0.27}_{-0.27}$	$8.20^{+0.75}_{-0.72}$	$0.170^{+0.050}_{-0.170}$	0.72 ± 0.14	1.4
HPS189	2.45	$8.64^{+0.18}_{-0.19}$	$7.63^{+0.33}_{-0.34}$	$0.073^{+0.014}_{-0.012}$	0.94 ± 0.06	1.0
HPS194	2.29	$9.28^{+0.28}_{-0.33}$	$8.16^{+0.47}_{-0.59}$	$0.046^{+0.015}_{-0.046}$	1.96 ± 0.07	7.9
HPS197	2.44	$7.83^{+0.35}_{-0.31}$	$6.91^{+0.88}_{-1.01}$	$0.093^{+0.022}_{-0.093}$	0.57 ± 0.11	1.1
HPS205	2.91	$8.70^{+0.48}_{-0.50}$	$8.37^{+0.66}_{-0.68}$	$0.068^{+0.002}_{-0.068}$	1.55 ± 0.53	6.2
HPS207	2.71	$7.99^{+0.36}_{-0.38}$	$7.39^{+0.64}_{-0.60}$	$0.045^{+0.010}_{-0.045}$	0.97 ± 0.17	2.8
HPS210	3.49	$8.23^{+0.31}_{-0.31}$	$7.26^{+0.50}_{-0.47}$	$0.013^{+0.002}_{-0.013}$	1.59 ± 0.26	3.1
HPS213	3.30	$9.90^{+0.18}_{-0.21}$	$9.01^{+0.27}_{-0.25}$	$0.020^{+0.004}_{-0.020}$	1.39 ± 0.06	9.3
HPS214	3.30	$7.95^{+0.53}_{-0.44}$	$6.94^{+1.09}_{-1.12}$	$0.125^{+0.028}_{-0.125}$	0.79 ± 0.25	0.4
HPS223	2.31	$8.19^{+0.36}_{-0.36}$	$7.94^{+0.50}_{-0.49}$	$0.029^{+0.004}_{-0.029}$	3.61 ± 0.54	3.2
HPS229	3.04	$9.80^{+0.11}_{-0.10}$	$8.41^{+0.15}_{-0.14}$	$0.015^{+0.003}_{-0.015}$	1.33 ± 0.03	6.3
HPS231	2.72	$7.89^{+0.27}_{-0.28}$	$7.65^{+0.40}_{-0.40}$	$0.031^{+0.006}_{-0.031}$	1.63 ± 0.21	2.1
HPS244	2.10	$7.64^{+0.15}_{-0.15}$	$6.38^{+0.57}_{-0.74}$	$0.070^{+0.014}_{-0.070}$	1.05 ± 0.16	0.5
HPS249	3.27	$9.06^{+0.24}_{-0.24}$	$7.62^{+0.38}_{-0.37}$	$0.266^{+0.019}_{-0.018}$	1.43 ± 0.17	3.0
HPS251	2.29	$8.40^{+0.29}_{-0.31}$	$7.57^{+0.40}_{-0.42}$	$0.025^{+0.006}_{-0.025}$	1.04 ± 0.05	4.4
HPS253	3.18	$8.81^{+0.25}_{-0.25}$	$7.60^{+0.35}_{-0.35}$	$0.020^{+0.005}_{-0.020}$	2.07 ± 0.10	2.1
HPS256	2.49	$8.17^{+0.19}_{-0.18}$	$7.28^{+0.31}_{-0.32}$	$0.041^{+0.010}_{-0.041}$	1.07 ± 0.07	2.9
HPS258	2.81	$8.94^{+0.17}_{-0.16}$	$7.87^{+0.26}_{-0.25}$	$0.022^{+0.005}_{-0.022}$	2.57 ± 0.06	7.3
HPS263	2.43	$8.88^{+0.18}_{-0.17}$	$7.60^{+0.34}_{-0.31}$	$0.049^{+0.012}_{-0.049}$	1.51 ± 0.05	3.8
HPS269	2.57	$8.87^{+0.17}_{-0.17}$	$8.25^{+0.27}_{-0.30}$	$0.035^{+0.008}_{-0.035}$	0.90 ± 0.07	3.0
HPS274	2.87	$9.06^{+0.12}_{-0.12}$	$7.45^{+0.21}_{-0.20}$	$0.120^{+0.009}_{-0.007}$	1.01 ± 0.02	4.3
HPS283	3.30	$9.65^{+0.16}_{-0.14}$	$8.59^{+0.24}_{-0.21}$	$0.027^{+0.006}_{-0.027}$	2.31 ± 0.10	2.8
HPS286	2.23	$8.94^{+0.25}_{-0.28}$	$8.11^{+0.37}_{-0.41}$	$0.024^{+0.004}_{-0.024}$	1.97 ± 0.10	24.3

Table 3—Continued

Galaxy ID	Redshift	Log Stellar Mass ($M_\odot$)	Log Age (yr)	$E(B-V)$	Half-light Radius (kpc)	χ^2_ν
HPS287	3.32	$8.77^{+0.30}_{-0.32}$	$7.47^{+0.48}_{-0.48}$	$0.207^{+0.020}_{-0.019}$	0.37 ± 0.21	1.3
HPS288	3.04	$8.77^{+0.28}_{-0.29}$	$7.31^{+0.48}_{-0.37}$	$0.039^{+0.010}_{-0.039}$	1.35 ± 0.04	0.8
HPS292	2.87	$8.59^{+0.19}_{-0.20}$	$7.71^{+0.28}_{-0.29}$	$0.022^{+0.006}_{-0.022}$	0.73 ± 0.04	5.8
HPS296	2.84	$8.26^{+0.21}_{-0.22}$	$7.51^{+0.30}_{-0.31}$	$0.011^{+0.002}_{-0.011}$	0.97 ± 0.11	9.4
HPS306	2.44	$9.01^{+0.12}_{-0.12}$	$7.73^{+0.21}_{-0.20}$	$0.039^{+0.009}_{-0.039}$	1.35 ± 0.04	3.3
HPS310	3.07	$9.26^{+0.22}_{-0.18}$	$8.54^{+0.32}_{-0.25}$	$0.024^{+0.004}_{-0.024}$	0.87 ± 0.05	4.1
HPS313	2.10	$9.82^{+0.08}_{-0.08}$	$7.74^{+0.11}_{-0.12}$	$0.161^{+0.007}_{-0.006}$	2.34 ± 0.02	17.3
HPS315	3.07	$9.04^{+0.23}_{-0.23}$	$7.42^{+0.37}_{-0.34}$	$0.096^{+0.011}_{-0.010}$	3.03 ± 0.09	2.0
HPS316	2.81	$9.40^{+0.11}_{-0.10}$	$8.28^{+0.19}_{-0.18}$	$0.027^{+0.006}_{-0.027}$	1.26 ± 0.03	1.9
HPS318	2.46	$9.54^{+0.12}_{-0.12}$	$7.79^{+0.23}_{-0.23}$	$0.139^{+0.011}_{-0.010}$	2.42 ± 0.07	6.9
HPS338	2.60	$7.86^{+0.43}_{-0.30}$	$6.87^{+0.93}_{-1.05}$	$0.116^{+0.014}_{-0.116}$	3.52 ± 0.13	0.9
HPS341	2.93	$8.41^{+0.18}_{-0.19}$	$6.91^{+0.55}_{-0.55}$	$0.059^{+0.017}_{-0.059}$	2.53 ± 0.50	1.0
HPS360	2.92	$9.89^{+0.18}_{-0.19}$	$7.96^{+0.56}_{-0.53}$	$0.266^{+0.046}_{-0.017}$	1.61 ± 0.04	1.9
HPS370	3.18	$8.40^{+0.22}_{-0.22}$	$7.38^{+0.33}_{-0.32}$	$0.033^{+0.008}_{-0.033}$	0.94 ± 0.02	0.9
HPS372	2.76	$7.52^{+0.44}_{-0.39}$	$7.03^{+0.97}_{-1.18}$	$0.067^{+0.017}_{-0.067}$	0.36 ± 0.06	2.9
HPS389	2.59	$9.09^{+0.10}_{-0.10}$	$7.72^{+0.17}_{-0.17}$	$0.107^{+0.010}_{-0.008}$	1.28 ± 0.02	1.9
HPS391	2.96	$9.44^{+0.13}_{-0.15}$	$8.13^{+0.27}_{-0.33}$	$0.101^{+0.016}_{-0.015}$	0.96 ± 0.01	1.2
HPS395	2.27	$9.34^{+0.09}_{-0.08}$	$8.36^{+0.18}_{-0.17}$	$0.036^{+0.009}_{-0.036}$	3.79 ± 0.52	1.6
HPS402	2.97	$8.36^{+0.14}_{-0.12}$	$6.97^{+0.28}_{-0.21}$	$0.051^{+0.008}_{-0.008}$	1.87 ± 0.03	2.2
HPS403	3.18	$8.97^{+0.28}_{-0.30}$	$8.17^{+0.41}_{-0.46}$	$0.037^{+0.010}_{-0.037}$	2.70 ± 0.16	7.8
HPS415	3.37	$9.71^{+0.15}_{-0.18}$	$9.05^{+0.22}_{-0.21}$	$0.019^{+0.004}_{-0.019}$	1.09 ± 0.03	4.3
HPS419	2.23	$10.00^{+0.13}_{-0.12}$	$8.83^{+0.28}_{-0.25}$	$0.132^{+0.019}_{-0.014}$	1.67 ± 0.02	1.8
HPS420	2.93	$8.67^{+0.18}_{-0.18}$	$7.71^{+0.28}_{-0.28}$	$0.052^{+0.011}_{-0.052}$	0.56 ± 0.01	5.4
HPS426	3.40	$9.57^{+0.20}_{-0.20}$	$8.84^{+0.42}_{-0.30}$	$0.049^{+0.011}_{-0.049}$	0.70 ± 0.02	4.1
HPS428	3.34	$9.46^{+0.10}_{-0.11}$	$8.04^{+0.18}_{-0.20}$	$0.072^{+0.010}_{-0.009}$	1.93 ± 0.07	2.9
HPS434	2.27	$9.03^{+0.31}_{-0.26}$	$8.74^{+0.71}_{-0.56}$	$0.073^{+0.026}_{-0.073}$	1.03 ± 0.04	3.1
HPS436	2.42	$8.36^{+0.15}_{-0.16}$	$7.23^{+0.24}_{-0.26}$	$0.077^{+0.009}_{-0.007}$	1.78 ± 0.02	1.5
HPS447	3.13	$8.39^{+0.10}_{-0.11}$	$6.36^{+0.60}_{-0.74}$	$0.033^{+0.009}_{-0.033}$	3.60 ± 0.11	2.5
HPS462	2.21	$10.48^{+0.13}_{-0.11}$	$8.61^{+0.32}_{-0.29}$	$0.296^{+0.024}_{-0.020}$	1.38 ± 0.84	2.8
HPS466	3.24	$9.04^{+0.03}_{-0.03}$	$6.82^{+0.05}_{-0.04}$	$0.134^{+0.004}_{-0.004}$	1.51 ± 0.01	12.9
HPS474	2.27	$8.97^{+0.20}_{-0.20}$	$7.95^{+0.35}_{-0.33}$	$0.096^{+0.014}_{-0.010}$	1.18 ± 0.02	8.3